Editors' Suggestion

Measurement of non-Abelian gauge fields using multiloop amplification

Qing-Xian Lv,[1,2] Hong-Zhi Liu,[1] Yan-Xiong Du,[1,*] Lin-Qing Chen,[1] Meng Wang,[1] Jia-Hao Liang,[1] Zhao-Xin Fu,[1] Zi-Yuan Chen,[1] Hui Yan,[1,2,3,†] and Shi-Liang Zhu[1,2,‡]

[1]*Key Laboratory of Atomic and Subatomic Structure and Quantum Control (Ministry of Education), School of Physics, South China Normal University, Guangzhou 510006, China*

[2]*Guangdong Provincial Key Laboratory of Quantum Engineering and Quantum Materials, Guangdong-Hong Kong Joint Laboratory of Quantum Matter, South China Normal University, Guangzhou 510006, China*

[3]*Guangdong Provincial Engineering Technology Research Center for Quantum Precision Measurement, Frontier Research Institute for Physics, South China Normal University, Guangzhou 510006, China*

(Received 7 May 2023; accepted 4 August 2023; published 28 August 2023)

Non-Abelian gauge field plays a central role in understanding the geometrical and topological phenomena in physics. Here we experimentally induce a non-Abelian gauge field in the degenerate eigensubspace of a double-Λ four-level atomic system. The non-Abelian nature of the gauge field is detected through the measurement of the noncommutativity of two successive evolution loops. Then we theoretically propose and experimentally demonstrate a scheme to measure the non-Abelian gauge field through multiloop evolution and robust holonomic quantum gates. The demonstrated scheme offers the advantage of detecting the non-Abelian gauge field with amplification through multiloop evolution. Our results pave the way for an experimentally feasible approach to achieving high-resolution and high-precision measurements of the gauge fields.

DOI: 10.1103/PhysRevA.108.023316

I. INTRODUCTION

The coupling between quantum systems and gauge fields gives rise to a plethora of physical phenomena, including topological insulators and topological semimetals in condensed-matter systems, as well as the Aharonov-Bohm (AB) effect and geometric phases in quantum systems [1–4]. Novel physics involving non-Abelian gauge fields, such as the θ vacuum and the non-Abelian AB effect, have also been discovered [5–8]. To rigorously study these theories, it is necessary to manipulate the degenerate wave functions under the non-Abelian gauge potentials [9–16]. Additionally, accurately measuring the localized gauge fields, which remains a challenging task, is crucial for investigating the geometrical and topological phenomena in physics.

Linear response is one of the methods to measure the geometric quantum tensor in parameter space [17–24]. The imaginary component of this tensor is the gauge field (Berry curvature), while the real component is the metric [25]. By quenching the parameters, the deflection of the evolution trajectory can be used to measure the gauge field. This approach has been successfully demonstrated in cold atomic systems, including the non-Abelian version [26,27]. The linear response method offers the advantage of enabling the determination of field strength in a small quench region, thereby facilitating high-resolution measurements. However, breaking adiabaticity is necessary to achieve observable effects, which weakens the robustness against deviations in the control parameters. Cyclic evolution is another method for measuring gauge fields and it is resistant to both random noise and systematic errors, owing to the geometric nature of geometric phases. By traversing a closed path in parameter space, a quantum system acquires a geometric phase that is determined by the integral of the Berry curvature [4,15,28–31]. However, it has low resolution in parameter space since the enclosed area should be sufficiently large to accumulate an observable effect. The noncommutative Wilczek-Zee phases are measured in cold atomic systems [32] and in a classical system constructed by noncommutative optical elements [31]. However, the local non-Abelian field cannot be retrieved from the Wilczek-Zee phase in common cases due to the path-ordered integral. Therefore, precise measurement of non-Abelian gauge fields is still lacking in experimental studies.

In this paper we report an experiment on the measurement of non-Abelian gauge fields with double-Λ four-level cold atoms. In contrast to the conventional tripod systems [33–36], the degenerate subspace utilized in our experiments corresponds to the system's lowest eigenvalue, resulting in a longer coherence time for the exploration of non-Abelian gauge fields. We demonstrate that non-Abelian gauge fields can be measured from multiloop evolution with tiny loops in the parameter space since the multiloop evolution can enhance the accuracy of measurement results, enabling measurements to be taken within a smaller loop while maintaining the same level of precision. We significantly simplify the process of measuring non-Abelian gauge fields in parameter space. There is a gap between the use of dressed states in defining the gauge fields and measurement of only bare states. This

*yanxiongdu@m.scnu.edu.cn
†yanhui@scnu.edu.cn
‡slzhu@scnu.edu.cn

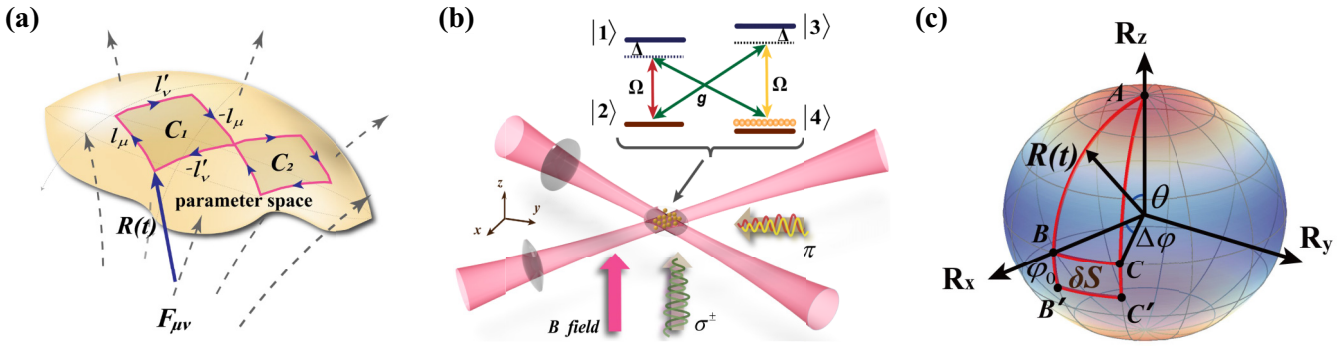

FIG. 1. (a) Measurement of non-Abelian gauge fields through the use of small loops in parameter space. (b) Experimental setup and coupling scheme. The double-Λ four-level Hamiltonian is realized in a cold ^{87}Rb atomic system: $|1\rangle = |F = 2, m_F = -1\rangle$, $|2\rangle = |F = 1, m_F = -1\rangle$, $|3\rangle = |F = 2, m_F = 0\rangle$, and $|4\rangle = |F = 1, m_F = 0\rangle$. (c) Measurement of non-Abelian gauge fields in a square loop of *B*-*B*′-*C*′-*C*-*B* is carried out by analyzing the difference in evolution between two triangles *A*-*B*-*C*-*A* and *A*-*B*′-*C*′-*A*

presents a significant challenge in experimental settings. We devise a scheme to measure the gauge field by utilizing the difference between two triangle loops that enclose the square loop. Both triangle loops originate and terminate at the pole of the Bloch sphere and the dressed states match the bare states at the beginning and end of the evolution. Consequently, the projective measurement of dressed states can be converted to bare states. We establish a connection between holonomic quantum gates and non-Abelian gauge fields and thus our method is robust against systematic errors and random noise. Therefore, our work provides a practical experimental method for attaining accurate and precise measurements of gauge fields.

The paper is organized as follows. In Sec. II we introduce our scheme to extract information about non-Abelian gauge fields from evolution operators. In Sec. III we illustrate a four-lever system with a twofold-degenerate eigensubspace and calculate the related non-Abelian gauge fields, which is a typical example of how these fields can emerge within a particular system. In Sec. IV we show a method to detect the non-Abelian gauge fields in a square loop process. In Sec. V we discuss the implications of our measurement effects of these gauge fields amplified by a multiloop evolution. This has an impact on the accuracy and validity of our measurements. In Sec. VI we study and visually demonstrate the change in population dynamics resulting from multiloop evolution. In Sec. VII we describe the measurement results of non-Abelian gauge fields. A brief summary is presented in Sec. VIII. In the Appendix we address the noncommutative nature of non-Abelian gauge fields and describe the experimental procedures and techniques utilized in our study to add transparency to our research.

II. NON-ABELIAN GAUGE FIELDS IN TINY LOOPS

We begin by addressing how to measure non-Abelian gauge fields with cyclic evolution. Considering a Hamiltonian $H(\mathbf{R}(t))$, with a doubly degenerate eigensubspace labeled by $\{|D_1\rangle, |D_2\rangle\}$, the non-Abelian gauge fields are given by $F_{\mu\nu} = \partial_\mu A_\nu - \partial_\nu A_\mu - i[A_\mu, A_\nu]$, where the gauge potential $A_\mu^{jk} = i\langle D_j|\partial_\mu|D_k\rangle$ $(j, k = 1, 2)$ and μ and ν are the components of driving parameter $\mathbf{R}(t)$ [9]. When the system controlled by the Hamiltonian $H(\mathbf{R}(t))$ evolves adiabatically along a closed path, the evolution operator U is given by a path-ordered integral

$$U = 1 - \int_0^s A_\mu d\mu + \int_0^s \int_0^{s'} A_\mu A_\nu d\mu\, d\nu + O(\mu^3), \quad (1)$$

where s and s' $(s' \leqslant s)$ are upper bounds of integral. Here we have omitted a global dynamical phase under the adiabatic assumption [9,28]. By considering a small loop $\mathbf{R}(t)$, $\mathbf{R}(0) \to \mathbf{R}(0) + \mathbf{l}_\mu \to \mathbf{R}(0) + \mathbf{l}_\mu + \mathbf{l}'_\nu \to \mathbf{l}_\mu + \mathbf{l}'_\nu \to \mathbf{R}(0)$, in the parameter space, as shown in Fig. 1(a), we obtain

$$U' \approx 1 - iF_{\mu\nu}\delta S, \quad (2)$$

using the second-order approximation, where $\delta S = (\mathbf{l}_\mu \mathbf{l}'_\nu - \mathbf{l}'_\nu \mathbf{l}_\mu)/2$ is the enclosed area [37]. Hence, measuring the evolution operator of tiny loops allows us to obtain the gauge fields.

III. NON-ABELIAN GAUGE FIELDS IN A FOUR-LEVEL SYSTEM

Non-Abelian gauge fields can be induced in a four-level system through a double-Λ configuration with four microwaves, as shown in Fig. 1(b). The coupling Rabi frequencies between $|1\rangle, |2\rangle$ and $|3\rangle, |4\rangle$ are set to Ω, while those between $|1\rangle, |3\rangle$ and $|2\rangle, |4\rangle$ are set to g. Under the bare state basis $\{|1\rangle, |2\rangle, |3\rangle, |4\rangle\}$ and rotating-wave approximation, the Hamiltonian reads

$$H(t) = \frac{\hbar}{2}\begin{pmatrix} \Delta & \Omega e^{-i\varphi} & 0 & -g \\ \Omega e^{i\varphi} & -\Delta & -g & 0 \\ 0 & -g & \Delta & -\Omega e^{i\varphi} \\ -g & 0 & -\Omega e^{-i\varphi} & -\Delta \end{pmatrix}, \quad (3)$$

where Δ are the detunings defined by the difference between the microwave frequencies and the corresponding coupling levels and φ are the relative phases [38]. Here we have adopted the four-photon resonant condition [38]. The Hamiltonian (3) can be experimentally realized in a ^{87}Rb cold atomic system, where we encode four Zeeman sublevels in the ground states by $|1\rangle = |F = 2, m_F = -1\rangle$, $|2\rangle = |F = 1, m_F = -1\rangle$, $|3\rangle = |F = 2, m_F = 0\rangle$, and $|4\rangle = |F = 1, m_F = 0\rangle$, respectively. A magnetic field about 0.5 G is applied to resolve the degeneracy of the Zeeman levels. Here $|1\rangle, |2\rangle$ and $|3\rangle, |4\rangle$ are coupled

by the π-transition microwaves while $|1\rangle$, $|4\rangle$ and $|2\rangle$, $|3\rangle$ are coupled by the σ- and σ^+-transition microwaves, respectively. The Rabi frequencies, frequencies, and phases of microwaves are all adjustable, which offers a fully controllable Hamiltonian. The system is initialized to state $|4\rangle$, which is realized by optically pumping atoms to $|3\rangle$ and then transferring to $|4\rangle$ by microwaves with a π pulse. A more detailed description of the experimental setup can be seen in Ref. [38].

The Hamiltonian (3) yields two twofold-degenerate eigenvalues: $\lambda_1 = \lambda_2 = -\Omega_0$ $(=-\sqrt{\Omega^2 + g^2 + \Delta^2})$, with the corresponding eigenstates $|D_1\rangle and |D_2\rangle$, and $\lambda_3 = \lambda_4 = \Omega_0$, with the corresponding eigenstates $|B_1\rangle and |B_2\rangle$. By parametrizing $\Omega = \Omega_0 \sin\theta\cos\phi$, $g = \Omega_0 \sin\theta\sin\phi$, and $\Delta = \Omega_0\cos\theta$, the eigenstates of the Hamiltonian (3) corresponding to the eigenvalues $\lambda_1 = \lambda_2 = -\Omega_0$ are given by

$$\begin{aligned} |D_1\rangle &= \sin\frac{\theta}{2}|1\rangle - \cos\frac{\theta}{2}(\cos\phi e^{i\varphi}|2\rangle - \sin\phi|4\rangle), \\ |D_2\rangle &= -\sin\frac{\theta}{2}|3\rangle - \cos\frac{\theta}{2}(\sin\phi|2\rangle + \cos\phi e^{-i\varphi}|4\rangle), \end{aligned} \tag{4}$$

while the eigenstates corresponding to the eigenvalues $\lambda_3 = \lambda_4 = \Omega_0$ are given by

$$\begin{aligned} |B_1\rangle &= -\sin\frac{\theta}{2}|2\rangle - \cos\frac{\theta}{2}(\cos\phi e^{-i\varphi}|1\rangle - \sin\phi|3\rangle), \\ |B_2\rangle &= \sin\frac{\theta}{2}|4\rangle - \cos\frac{\theta}{2}(\sin\phi|1\rangle + \cos\phi e^{i\varphi}|3\rangle). \end{aligned} \tag{5}$$

It is important to note that the degenerate eigenstates previously proposed to generate non-Abelian gauge fields in three-level atoms do not correspond to the lowest energy level [33–36]. In contrast, here we demonstrate that non-Abelian gauge fields $F_{\mu\nu}$, where $\mu, \nu = \theta, \phi, \varphi$, can be obtained from the lower eigenstates $|D_1\rangle and |D_2\rangle$. One will obtain the non-Abelian gauge potentials as $\mathbf{A} = (A_\theta, A_\phi, A_\varphi)$, with

$$\begin{aligned} A_\theta &= 0, \\ A_\phi &= -i\cos^2(\theta/2)\kappa_\phi\cdot\sigma, \\ A_\varphi &= i\cos^2(\theta/2)\cos\phi\kappa_\varphi\cdot\sigma, \end{aligned} \tag{6}$$

where $\sigma = (\sigma_x, \sigma_y, \sigma_z)$, with $\sigma_{x,y,z}$ the Pauli matrixes. The unit vectors $\kappa_\phi = (-\sin\varphi, \cos\varphi, 0)$ and $\kappa_\varphi = (-\sin\phi\cos\varphi, \sin\phi\sin\varphi, \cos\phi)$. Components of the non-Abelian gauge fields along two of the coordinates θ, φ, and ϕ are given by

$$\begin{aligned} F_{\theta\varphi} &= -i\sin\theta\cos\phi\kappa_{\theta\varphi}\cdot\sigma/2, \\ F_{\theta\phi} &= \sin\theta\kappa_{\theta\phi}\cdot\sigma/2, \\ F_{\phi\varphi} &= 2\cos^2(\theta/2)[1-\cos^2(\theta/2)]\cos\phi\kappa_{\phi\varphi}\cdot\sigma, \end{aligned} \tag{7}$$

where the unit vectors $\kappa_{\theta\varphi} = (\sin\phi\cos\varphi, \sin\phi\sin\varphi, \cos\phi)$, $\kappa_{\theta\phi} = (\sin\varphi, -\cos\varphi, 0)$, and $\kappa_{\phi\varphi} = (\cos\phi\cos\varphi, \cos\phi\sin\varphi, \sin\phi)$. Similar results can be found in the upper eigensubspace $\{|B_1\rangle, |B_2\rangle\}$. Without loss of generality, we will focus on the gauge field with the parameters θ and φ. We note that $F_{\theta\varphi}$ is associated with the infinitesimal $d\theta d\varphi$ in Cartesian coordinates. When we switch to spherical coordinates with an infinitesimal area $\sin\theta d\theta d\varphi$, the non-Abelian gauge field is given by

$$F^S_{\theta\varphi} = F_{\theta\varphi}/\sin\theta = -i\cos\phi\kappa_{\theta\varphi}\cdot\sigma/2, \tag{8}$$

which is obviously an SU(2) monopole.

The non-Abelian nature of gauge fields can be identified by the noncommutativity of two successive loops in parameter space, as shown by C_1 and C_2 in Fig. 1(a). If we denote the evolution operator of C_1 (C_2) by U_1 (U_2), the evolution operator of composite paths with order C_1C_2 (counterorder C_2C_1) will be given by $U_o = U_2U_1$ ($U_{co} = U_1U_2$). In Sec. 1 of the Appendix we demonstrate that the inequality $U_2U_1 \neq U_1U_2$ can be verified through experimental data obtained by measuring nondiagonal matrix elements $|U_o^{12\,(21)}|^2 \neq |U_{co}^{12\,(21)}|^2$ [28]. These matrix elements are determined by the population transfers after evolution and can be detected in our experiments. As a result, we have experimentally confirmed the existence of a true non-Abelian gauge field in this four-level atomic system.

IV. DETECTING NON-ABELIAN GAUGE FIELDS IN SQUARE LOOPS

As shown in Fig. 1(c), we present our method for measuring the gauge field within the region $\delta S' = \Delta\theta\Delta\varphi$ enclosed by the square loop B-B'-C'-C-B. However, it should be noted that the gauge fields are defined in the eigensubspace $\{|D_1\rangle, |D_2\rangle\}$, which cannot be directly measured. To reduce the experimental challenge, it would be more convenient to measure the population of bare states $\{|1\rangle, |2\rangle, |3\rangle, |4\rangle\}$. We employ two triangle loops [as labeled by A-B-C-A and A-B'-C'-A in Fig. 1(c)] to extract the non-Abelian gauge field in the loop B-B'-C'-C-B, with the following parameter settings: For $\theta(t)$, $0 \to \theta_0 \to 0$, and for $\varphi(t)$, $\varphi_0 \to \varphi_0 + \Delta\varphi$. In the Appendix we demonstrate that the eigenstates coincide with the bare states at the starting and ending points, based on the aforementioned parameter settings. As a result, the tomography of the eigenstates can be transformed to that of the bare states. Additionally, due to the gauge potentials along the longitude line always vanishing and not contributing to the line integral in Eq. (1), i.e., $A_\theta = 0$, one can select appropriate paths with a sufficiently large area to accumulate a considerable observable effect. In this case, the effective gauge field of the square loop is given as

$$\bar{F}_{\theta\varphi}(\theta_0, \varphi_0) = \begin{pmatrix} \bar{F}^{11}_{\theta\varphi} & \bar{F}^{12}_{\theta\varphi} \\ \bar{F}^{21}_{\theta\varphi} & \bar{F}^{22}_{\theta\varphi} \end{pmatrix} \approx \frac{U_2 - U_1}{i\delta S'}, \tag{9}$$

where U_1 (U_2) is the evolution operator of the triangle loop A-B-C-A (A-B'-C'-A). The second-order approximation in Eq. (2) is valid when the angle $\Delta\varphi \ll \pi$.

V. AMPLIFYING THE EFFECT OF NON-ABELIAN GAUGE FIELDS BY MULTILOOP APPROACH

The distinction between U_1 and U_2 may not be detectable if the gauge field within the loop B-B'-C'-C-B is not sufficiently large. However, a significant advantage of the current method is that we can enhance the influence of the gauge field by iterating the progression of the loop A-B-C-A (A-B'-C'-A), resulting in a more precise measurement. By utilizing the multiplicity, the evolution operator for N loops can be expressed as $U_N = (U')^N$. Hence, if U_N can be measured, the evolution operator for a single loop can be derived as $U' = U_N^{1/N}$, enabling the retrieval of non-Abelian gauge fields. Furthermore, the evolution operator of the triangle loop can be analytically

obtained by solving the Schrödinger equation, which is given by

$$U^g = \begin{pmatrix} \cos\kappa e^{i\beta} & i\sin\kappa e^{-i\beta} \\ i\sin\kappa e^{i\beta} & \cos\kappa e^{-i\beta} \end{pmatrix}. \tag{10}$$

Substituting Eq. (10) into the Schrödinger equation and expanding the quantum state by $|\Psi\rangle = c_1|D_1\rangle + c_2|D_2\rangle$, we have

$$\dot{U}^g = -A_\varphi \dot{\varphi} U^g, \tag{11}$$

where the overdot means derivation over time t. By adopting the triangle loop model in Fig. 1(c), we will obtain

$$\begin{aligned} \beta = -\alpha &= \cos^2\phi \oint \cos^2(\theta/2) d\varphi = \cos^2\phi \Delta\varphi, \\ \kappa &= \cos\phi\sin\phi \oint \cos^2(\theta/2) d\varphi = \cos\phi\sin\phi\Delta\varphi, \end{aligned} \tag{12}$$

where $\Delta\varphi$ is the angle of the triangle loops. One can further deduce

$$U^g = e^{i\eta\vec{h}\cdot\sigma}, \tag{13}$$

where $\vec{h} = (\sin\chi\cos\xi, \sin\chi\sin\xi, \cos\chi)$, $\xi = \beta$, $\tan\chi = \tan\kappa/\sin\beta$, and $\sin\eta = \sqrt{\sin^2\kappa + \cos^2\kappa\sin^2\beta}$. The evolution can be viewed as the quantum state circling around the axis $\vec{h}$ by an angle of η once (and $N\eta$ for N triangle loops). When $\Delta\varphi \ll \pi$, we have $\sin\kappa \sim \kappa$ and $\cos\kappa \sim 0$; thus Eq. (10) can be modified as

$$U^g = \begin{pmatrix} 1 - i\beta & i\kappa e^{-i\beta} \\ i\kappa e^{i\beta} & 1 + i\beta \end{pmatrix}. \tag{14}$$

Meanwhile, according to Eq. (2), we have $U' = 1 - \bar{F}_{\theta\varphi}(\Delta\varphi)\Delta S = 1 - \iint F_{\theta\varphi} d\theta\, d\varphi$, which can easily recover the result of Eq. (10) for $\Delta\varphi \ll \pi$ and $\phi \ll \pi$. Therefore, by measuring the evolution of the triangle loops model, specifically the geometric gate, we can detect the non-Abelian gauge field. It can be found that $U' = U^g$ when $\Delta\varphi \ll \pi$. Furthermore, U^g is a geometric gate utilized in adiabatic Holonomic quantum computation [39–45], which rotates the quantum state along a specific axis in the Hilbert space. As a result, the Nth root of the evolution operator U_N can be comprehended as extracting a rotation angle from N consecutive rotations. We thus establish a connection between holonomic quantum gates and non-Abelian gauge fields.

VI. EXPERIMENTAL CONTROL AND THE AMPLIFICATION EFFECT

We conduct experiments on a four-level atomic system, as depicted in Fig. 1(b). The atoms are confined within an optical dipole trap and cooled to a temperature of 10 μK via evaporation. A magnetic field is applied along the z axis to establish the quantization axis, resulting in a frequency difference of 700 kHz between the Zeeman levels. The experimental parameters are chosen to be $\Omega_0 = 2\pi \times 50$ kHz and $T = 450$ μs, satisfying the adiabatic condition $\Omega_0 T = 45\pi \gg 2\pi$. To introduce intermediate coupling g, we keep $\phi = \pi/8$. The Allen-Eberly scheme [46] is used to drive $\theta(t)$, which has the form

$$\theta(t) = \begin{cases} \theta_0\{1 + \tanh[b(t - T/4)]\}/2, & t \in [0, T/2) \\ \theta_0\{1 - \tanh[b(t - 3T/4)]\}/2, & t \in [T/2, T], \end{cases} \tag{15}$$

where $b = 10/T$. Here $\Delta\varphi = 0.1\pi$ is chosen to meet the second-order approximation.

We will now discuss the amplification effect resulting from multiloop evolution. The experiments are conducted as follows. First, an initial state of $|\Psi\rangle_i = |4\rangle$ is prepared. The system is then driven to evolve along the closed path *A*-*B*-*C*-*A* (*A*-*B*′-*C*′-*A*) and the final population P_4 remaining in $|4\rangle$ is measured and the results are plotted in Fig. 2(a). The experimental data agree well with the theoretical calculations. Although the control parameter $\theta(t)$ returns to the initial value at the end, the population does not revert to its initial state. This is due to the non-Abelian geometric phase induced in the degenerate subspace. The population decline is more rapid when $\theta = 0.6\pi$ compared to $\theta = 0.5\pi$ because the former has a larger enclosed area. In our experiments, the standard deviation of the experimental data approaches 0.011 after 20 iterations of averaging. To better visualize the amplification effect of multiloop evolution, we plot the population of P_4 at the end of each loop in Fig. 2(b). For the case of $\theta_0 = 0.5\pi$, the value of P_4 at the end of the first loop ($N = 1$) is almost indistinguishable from 1. However, as the loops progress, P_4 decreases to 0.94(3) by the fifth loop, which is easily detectable in our experimental system. Similar results are observed for the case of $\theta_0 = 0.6\pi$. Hence, the impact of non-Abelian gauge fields can be magnified through a multiloop approach. Nonetheless, the maximum number of loops is constrained by the coherent time and flight time of the atomic system upon release. In our particular system, the Zeeman levels have a coherence time of approximately 4 ms. Consequently, we have established a maximum of five cycles, in accordance with the evolution period of $T = 450$ μs.

We subsequently address the minimum detectable area in our experiments. Given the spherically symmetric nature of the non-Abelian gauge field and the fact that the enclosed flux is independent of both position and shape, we specify the triangle loop [*A*-*B*-*C*-*A* in Fig. 1(c)] to discuss this issue. By setting $\theta_0 = 0.5\pi$ and scanning $\Delta\varphi$, we can tilt the enclosed area $\delta S'$. The criterion for determining the minimal area can be determined by the minimal detectable population difference of P_4, which is 0.011 according to the standard derivation. When preparing the system for the state $|4\rangle$, the population P_4 versus $\delta S'$ with $N = 1, 3, 5$ is plotted in Fig. 2(c). While the minimum area required for a single loop ($N = 1$) is approximately 0.2π, the minimum area required for five loops ($N = 5$) is only about 0.05π. Increasing the number of loops in the evolution process can therefore improve the measurement resolution of gauge fields.

VII. MEASUREMENT RESULTS OF NON-ABELIAN GAUGE FIELDS

We will now describe a state tomography method to extract the non-Abelian gauge fields. Since the parameter $\theta(t)$

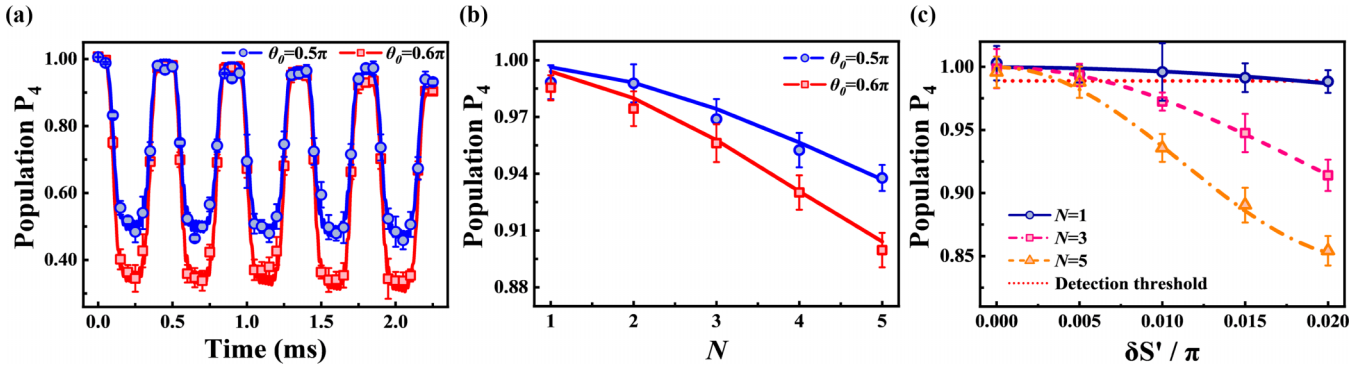

FIG. 2. Performance of the multiloop approach. (a) Population P_4 in state $|4\rangle$ for $N = 5$. The data have been averaged over 10 times. (b) Final population P_4 for $N = 1$–5. The data have been averaged 20 times. The amplification effect is demonstrated since the population decreases with N. (c) Minimal enclosing area that can be detected. The threshold of minimal population deviation is set to 0.01 according to the limitation of the error bar calculation from numerous measurements. The minimal enclosing area decreases as the number of loops increases where the minimal enclosing area of $N = 5$ loops is 4 times smaller than that of $N = 1$ loop.

evolves adiabatically with $\theta(0) = \theta(T) = 0$, the initial state and the final state are restricted inside the subspace spanned by $\{|2\rangle, |4\rangle\}$, which can be regarded as a pseudospin $\mathbf{F}$ [47]. We define the final state as $|\Psi\rangle_f = a_1|2\rangle + b_1|4\rangle$ ($|\Psi'\rangle_f = a_2|2\rangle + b_2|4\rangle$) when the initial state is $|\Psi\rangle_i = |2\rangle$ ($|\Psi'\rangle_i = |4\rangle$); then the N loops evolution operator is given by $U_N = \begin{pmatrix} a_1 & b_1 \\ a_2 & b_2 \end{pmatrix}$, where $a_2 = -b_1^*$ and $b_2 = a_1^*$ to keep U_N unitary. As shown in the Appendix, $|a_1| = 2\langle\sigma_z\rangle - 1$ and $\arg(b_1) - \arg(a_1) = \arctan(\langle\sigma_y\rangle/\langle\sigma_x\rangle)$, where $\arg(x)$ gives the phase of the complex number x. Hence, a_l and b_l ($l = 1, 2$) can be obtained by taking the tomography of the pseudospin $\mathbf{F}$ [48]. In the Appendix we show that our tomograph is based on nonadiabatic holonomic quantum gates.

In Fig. 3(a) the final state tomography upon evolution along the triangle loop with $\theta = 0.5\pi$ and $\Delta\varphi = 0.1\pi$ is plotted. It can be seen that $\mathbf{F}$ rotates around a specific axis determined by U^g. The experimental results of the first five loops are represented by the black stars in Fig. 3(a), where the data of the fifth loop are obtained as $\langle\sigma_x\rangle_5 = 0.334$, $\langle\sigma_y\rangle_5 = 0.299$, and $\langle\sigma_z\rangle_5 = -0.894$. According to the formulation of U_N, the evolution operator $U_5(0.5\pi, 0.1\pi)$ of five loops can be obtained and the single-loop evolution operator is obtained as $U(0.5\pi, 0.1\pi) = U_5^{1/5}(0.5\pi, 0.1\pi)$.

We continue to compute the matrix elements of the gauge fields in the loop B-B'-C'-C-B depicted in Fig. 1(c). We select the parameters $\Delta\theta = 0.1\pi$ and $\Delta\varphi = 0.1\pi$. According to Eq. (5), the non-Abelian gauge fields are given by $\bar{F}_{\theta\varphi}(\theta_0, \varphi_0) = [U(\theta_0 + \Delta\theta, \varphi_0 + \Delta\varphi) - U(\theta_0, \varphi)]/\delta S'$, of which the evolution operators U are traced by a five-loop evolution. The experimental results along the $\varphi_0 = 0$ longitude line are shown in Fig. 3(b). The experimental data appear to be sinusoidal and fit well with the theoretical simulation. Here the nonvanishing nondiagonal elements $|\bar{F}^{12}_{\theta\varphi}|$ clearly show the non-Abelian characteristic of the measured gauge fields. As mentioned before, $\bar{F}_{\theta\varphi}$ is defined in the Cartesian coordinates with $\delta S' = \Delta\theta\Delta\varphi$. To recover the characteristic of the SU(2) monopole (independent of the field angles), we plot the data of $\bar{F}^S_{\theta\varphi} = \bar{F}_{\theta\varphi}/\sin\theta$ which is shown in Fig. 3(c).

VIII. CONCLUSION

In summary, we have theoretically proposed and experimentally demonstrated an approach to measure non-Abelian

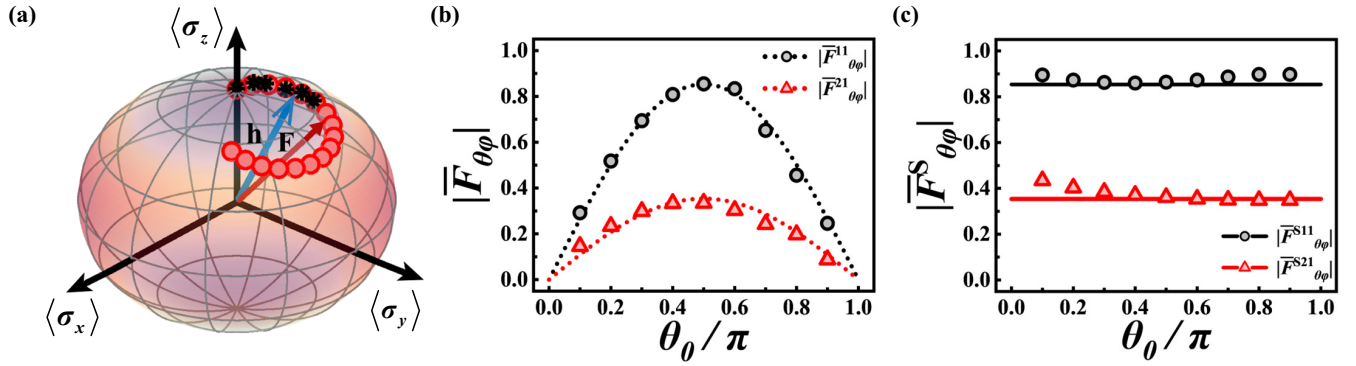

FIG. 3. (a) Tomographic results of pseudospin $\mathbf{F}$ at the end of N loops. Black stars denote experimental results of $N = 1$–5 and red circles the theoretical simulation of $N = 1$–17 loops. Pseudospin $\mathbf{F}$ rotates along the axis $\mathbf{h}$ determined by the geometric gate U_g. (b) Experimental results of non-Abelian gauge fields. The black dotted line with circles shows results for $|\bar{F}^{11}_{\theta\varphi}|$ and the red dotted line with triangles shows $|\bar{F}^{21}_{\theta\varphi}|$. The experimental data have been average for 20 measurements and the error bars are too small to be shown. (c) Refined gauge field in the spherical coordinates. The black solid line with circles shows results for $|\bar{F}^{S11}_{\theta\varphi}|$ and the red solid line with triangles shows $|\bar{F}^{S21}_{\theta\varphi}|$.

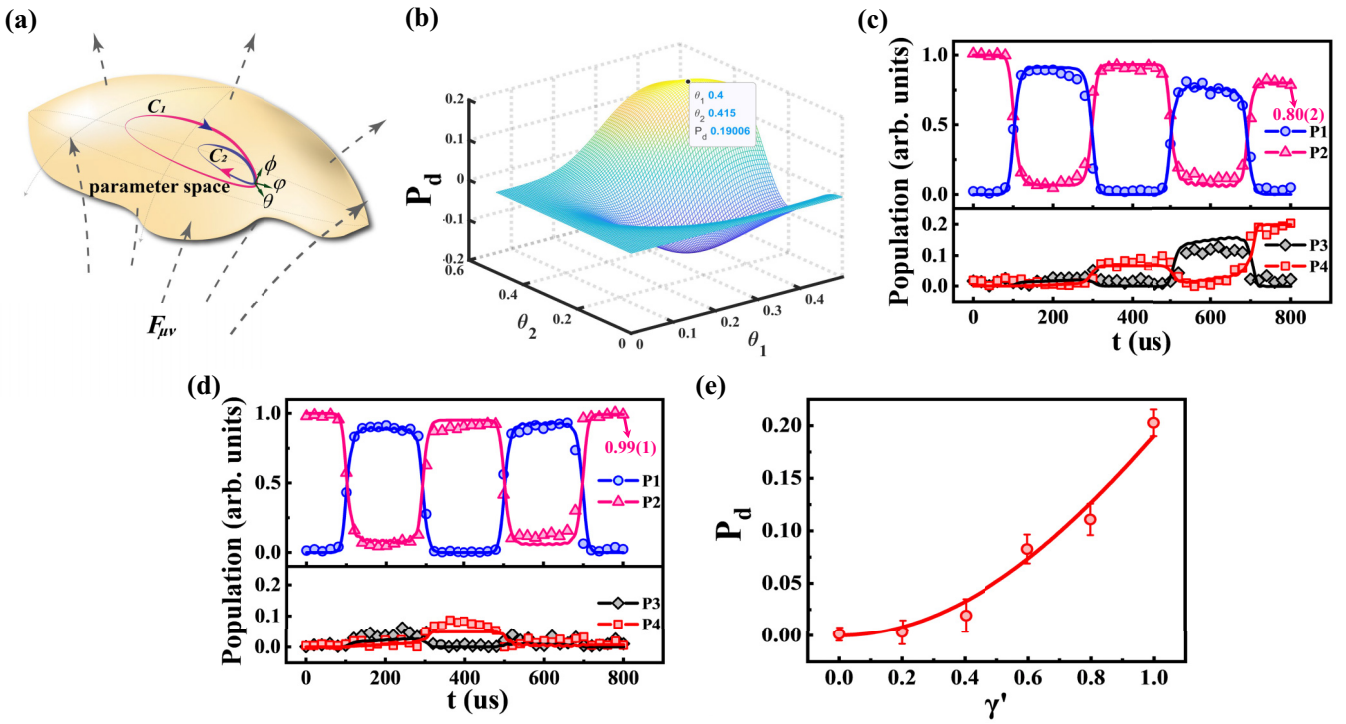

FIG. 4. Measurements of noncommutativity of non-Abelian gauge fields. (a) A quantum system undergoing cyclic and adiabatic evolution in the parameter space will acquire a Wilczek-Zee phase that is associated with a non-Abelian gauge field $F_{\mu\nu}$. The commutativity of the gauge field can be detected by observing the final population difference resulting from changing the order of two successive closed loops. (b) Population difference versus the parameters θ_1 and θ_2 in C_1 and C_2, respectively. The population dynamics is shown for evolutions (c) C_1C_2 and (d) C_2C_1 at $\gamma' = 1$. Pink triangles, blue circles, red squares, and gray diamonds denote experimental results for population at each level $|i\rangle(P_i)$, $i = 1, 2, 3, 4$, respectively, which have been averaged for five measurements. Solid lines show simulation results. (e) Difference in final population left in $|4\rangle$ between composite loops $C_1C_2(P_{12})$ and $C_2C_1(P_{21})$. A nonvanishing population difference corresponds to the non-Abelian characteristic while a vanishing population difference corresponds to the Abelian one. The gauge fields can change from non-Abelian to Abelian by tilting the parameter γ'. Red circles with error bars show experimental data which have been averaged by ten measurements and the red solid line is the simulation curve.

gauge fields. This method offers the advantage of amplification through multiloop evolution. Moreover, we can accelerate the manipulation by incorporating a shortcut to adiabaticity through the addition of an auxiliary Hamiltonian [49–54]. Our results have the potential to be applied in various studies of geometrical and topological phenomena in quantum systems.

ACKNOWLEDGMENTS

The authors thank Z.-Y. Wang for helpful discussions. This work was supported by the Science and Technology Program of Guangzhou (Grant No. 202201010533), the China Postdoctoral Science Foundation (Grants No. 2022M721222 and No. 2023T160233), the Guangdong Basic and Applied Basic Research Foundation (Grants No. 2021A1515110668 and No. 2023A1515011550), the National Key Research and Development Program of China (Grants No. 2022YFA1405300, No. 2022YFA1405303, and No. 2020YFA0309500), the National Natural Science Foundation of China (Grants No. 12074132, No. 12225405, No. 12247123, No. 12304287, No. U20A2074, and No. 12074180), and the Innovation Program for Quantum Science and Technology (Grant No. 2021ZD0301705).

Q.-X.L, H.-Z.L., and Y.-X.D contributed equally to this work.

APPENDIX: EXPERIMENTAL DETAILS

1. Testing the noncommutation of non-Abelian gauge fields

The non-Abelian gauge fields can be induced in the degenerate eigensubspaces. To confirm the generation of non-Abelian gauge field in this four-level system, it is necessary to examine its major characteristic, which is noncommutativity. The noncommutativity of $F_{\mu\nu}$ can be detected by analyzing the corresponding cyclic evolution operator U^c associated with A_μ [28],

$$U^c = \begin{pmatrix} U^{11} & U^{12} \\ U^{21} & U^{22} \end{pmatrix} = \hat{P} e^{-\oint_c A_\mu d\mu}, \tag{A1}$$

where $\hat{P}$ represents the path-ordered operator. As shown in Fig. 4(a), two different loops C_1 and C_2 formed by the vector $\mathbf{R}(\theta, \phi, \varphi)$ in parameter space are adopted. Assuming that the evolution operators of C_1 and C_2 are given by U_1 and U_2, respectively, then the evolution operators of composite paths with order C_1C_2 and counterorder C_2C_1 will be given by $U_o = U_2U_1$ and $U_{co} = U_1U_2$, respectively. Here $U_2U_1 \neq U_1U_2$ can be validated by the nondiagonal matrix elements $|U_o^{12\,(21)}|^2 \neq |U_{co}^{12\,(21)}|^2$, namely, the population transfers after evolution. It should be noted that the starting points of C_1 and C_2 must coincide; otherwise, two loops with disconnected

starting points may be treated as two noncommutative gates in geometric quantum computation.

To realize two different loops in parameter space, the parameters θ, ϕ, and φ of C_1 and C_2 can be specified as $\theta^{(1\ (2))} = \theta_{1\ (2)} f(t)$, $\phi^{(1)} = \phi^{(2)} = \gamma f(t)$, $\varphi^{(1)} = 2\pi t/T$, and $\varphi^{(2)} = 2\pi f(t)t/T$, where T is the evolution period. By setting $f(t : 0 \to T) : 0 \to 0$, the Hamiltonian (3) satisfies $H(0) = H(T)$, which experiences cyclic evolution in parameter space. Here we choose to tilt θ, ϕ, and φ simultaneously since $F_{\theta\varphi}$, $F_{\theta\phi}$, and $F_{\phi\varphi}$ are all nonvanishing.

One of the primary challenges in testing noncommutativity is the need to detect the population of eigenstates, as the gauge fields are defined within their respective subspaces. However, this obstacle can be overcome by selecting appropriate parameter settings. It is evident from Eqs. (4) and (5) that, with the provided loops C_1 and C_2, the association between eigenstates and bare states can be elucidated as follows:

$$\begin{aligned} |D_1(t=0)\rangle &= |D_1(t=T)\rangle = |2\rangle, \\ |D_2(t=0)\rangle &= |D_2(t=T)\rangle = |4\rangle, \\ |B_1(t=0)\rangle &= |B_1(t=T)\rangle = |1\rangle, \\ |B_2(t=0)\rangle &= |B_2(t=T)\rangle = |3\rangle. \end{aligned} \tag{A2}$$

Hence, by detecting the population of the bare states under suitable conditions, one can easily detect the population of the eigenstates, thereby significantly reducing the experimental challenge.

The experiments conducted to examine noncommutativity are carried out as follows. First, we prepare the initial state of the system to be $|\Psi\rangle_i = |4\rangle = |D_2\rangle$. Next we drive the system to evolve along the closed paths C_1 and C_2 and measure the population $P_{12} = |U_{\rm o}^{12}|^2$ transferred to $|2\rangle = |D_1\rangle$. In contrast, we drive the system to evolve along the closed paths C_2 and C_1 and measure the population $P_{21} = |U_{\rm co}^{12}|^2$ transferred to the state $|2\rangle$. For more detailed information on how to measure the population in the four-level system, refer to Ref. [38]. If the population difference $P_d = P_{12} - P_{21} \neq 0$, then $U_{\rm o} \neq U_{\rm co}$.

Just like the theoretical simulation shown in Fig. 4(b), we have set $\theta_1 = 0.4\pi$, $\theta_2 = 0.415\pi$, and $\gamma = \pi/16$ to achieve maximum population difference and noncommutativity. Note that all evolution must be adiabatic to ensure that the system remains in the lower subspace where the Rabi frequency $\Omega_0 = 2\pi \times 50$ kHz and $T = 400$ μs, satisfying the adiabatic condition $\Omega_0 T = 40\pi \gg 2\pi$. The population dynamics during the evolution of C_1C_2 and C_2C_1 are illustrated in Figs. 4(c) and 4(d), respectively. The pink triangles, blue circles, red squares, and gray diamonds represent the experimental data for population P_i at level $|i\rangle$, where $i = 1, 2, 3, 4$. Meanwhile, the solid lines depict the simulation results. The final population of $|2\rangle$ is 0.80(2) for C_1C_2 and 0.99(1) for C_2C_1.

Hence, it has been established through noncommutativity that the induced gauge fields must be non-Abelian. Additionally, the properties of the induced gauge fields can be modified by varying $\gamma' = \gamma/(\pi/16)$. In Fig. 4(e) it can be observed that when $\gamma' = 0$, the four-level system is reduced to two two-level systems, constructed by $\{|1\rangle, |2\rangle\}$ and $\{|3\rangle, |4\rangle\}$, respectively. Each of the two subsystems induces an Abelian field and thus there is no population difference. On the other hand, when $\gamma' = 1$, we arrive at the case depicted in Figs. 4(c) and 4(d). The total variation of P_d during the interval $\gamma' \in [0, 1]$ is illustrated in Fig. 4(e).

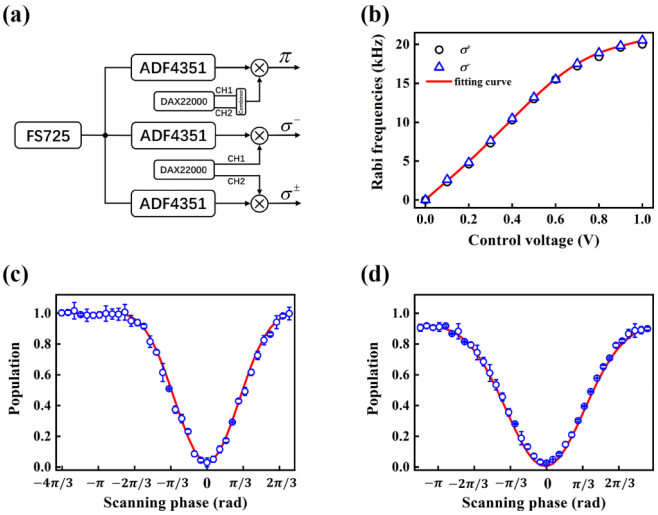

FIG. 5. Calibrating the phases and amplitudes of the microwaves. (a) Electronic circuits of the microwave system. To keep phase coherence between different microwaves, all eigensources are synchronized to the same atomic clock: FS725, the atomic clock; ADF4351, eigenmicrowave sources; and DAX22000, two-channel arbitrary waveform generator (CH1 and CH2). By mixing the signals from eigensources and radio sources, the arbitrary time-varying amplitude, frequency, and phase of the microwave field can be achieved. (b) Rabi frequencies of the intermediate coupling g controlled with $\sigma^{\pm}$. Black circles denote σ^+ and blue triangles σ^-. The red solid line is the fitting curve with a polynomial. The Rabi frequencies of σ^+ and σ^- can be adjusted to be equivalent at varying control voltages. The population difference is obtained by scanning the relative phases between two microwave pulses: (c) $\sigma^{\pm}$ versus π and (d) σ^- versus π. Red solid lines are the fitting curves with the form $f(\phi_{ab}) = \sqrt{\Omega_a^2 + \Omega_b^2 + 2\Omega_a\Omega_b \cos\phi_{ab}}$, where Ω_a and Ω_b are the Rabi frequencies and ϕ_{ab} is the relative phase. Blue dots with error bars show the experimental data.

2. Experimental setup

The experimental setup is shown in Fig. 1(b). Cold atoms are trapped in an optical dipole trap and cooled down to a temperature of 10 μK through evaporation. Three microwave horn antennas (here the σ^--polarized microwave horn antenna is omitted, which is used for initial-state preparation and quantum state tomography) are employed to couple different levels of ^{87}Rb. The two microwaves, which are individually π polarized, originate from a single linearly polarized microwave horn antenna. These microwaves are utilized to realize π transitions [that is, the transition between $|1\rangle$ ($|3\rangle$) and $|2\rangle$ ($|4\rangle$)]. Two additional $\sigma^{\pm}$-polarized microwaves, which stem from the σ^+-polarized microwave horn antenna, are not considered independent. This is because the antenna is not completely pure and there is backreflection from the surrounding environment, resulting in the production of σ^--polarized microwaves from the same antenna. Therefore, the $\sigma^{\pm}$ transition of the intermediate coupling, which refers to the transition between $|2\rangle$ ($|4\rangle$) and $|3\rangle$ ($|1\rangle$), can be achieved using only one circular

polarization horn antenna. As shown in Fig. 5(a), the microwave eigensources are generated by frequency synthesizers (Analog Devices, ADF4351) that are all connected to the same atomic clock. All horn antennas, including those polarized as π, $\sigma^{\pm}$, and σ^{-}, emit microwaves that are generated from a device (Waveponds, DAX22000-8M) through a process of mixing radio frequencies with their eigenfrequencies.

We introduce intermediate couplings between the two single qubits ($|1\rangle$, $|4\rangle$ and $|2\rangle$, $|3\rangle$) to induce non-Abelian gauge fields. The σ^{+} and σ^{-} transitions in the intermediate coupling should be equal according to the Hamiltonian (3), which can be realized by regulating the position of the $\sigma^{\pm}$ horn antenna. We prepared the system to be in the state $|2\rangle$ or $|4\rangle$ and measured the Rabi oscillation caused by the σ^{+} and σ^{-} transition microwaves, respectively. Based on the measured Rabi frequencies, we meticulously adjusted the position of the $\sigma^{\pm}$ horn antenna until the σ^{+} and σ^{-} transitions in the intermediate couplings were equal. The data for σ^{+} and σ^{-} transitions are presented in Fig. 5(b), which clearly illustrates that the Rabi frequencies of σ^{+} (represented by black circles) are equivalent to those of σ^{-} (represented by blue triangles) across varying control voltages. This confirms the successful achievement of intermediate coupling.

3. Calibration of the relative phases

To achieve the four-level Hamiltonian (3), precise calibration of the relative phases among the microwaves is essential. During the experiment, phase differences may arise due to various factors such as transport paths, electronic delays, and the radio frequencies used for initializing the microwave phases. To address this issue, we detect the relative phases of the microwaves by observing the interference between the Rabi frequencies of the corresponding microwaves. We begin by preparing the system in the initial state $|4\rangle$ and tuning two of the microwaves to be resonant with both $|4\rangle$ and $|3\rangle$. The resulting induced population is dependent on the synthetic Rabi frequency, which is determined by the phase difference between the Rabi frequencies of the two microwaves. By measuring the population, we can extract the relative phases between the microwaves.

In Figs. 5(c) and 5(d) the relative phases between the π-transition microwave and one of the $\sigma^{\pm}$ (σ^{-}) transitions are presented. The lowest population corresponds to zero phase difference. The experimental data are represented by blue circles with error bars, while the theoretical curves are depicted by red solid curves in the form of $f(\phi_{ab}) = \sqrt{\Omega_a^2 + \Omega_b^2 + 2\Omega_a\Omega_b\cos(\phi_{ab})}$. The Rabi frequencies are denoted by Ω_a and Ω_b and the relative phase is indicated by ϕ_{ab}. Finally, we adjust the phase of one microwave, specifically the π-transition microwave, and then align the phases of the $\sigma^{\pm}$- and σ^{-}-transition microwaves to meet the required phase conditions. We note that the two channels of the π-transition microwave are produced from the same source and transported along identical paths, resulting in their phases being automatically synchronized.

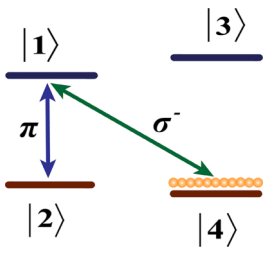

FIG. 6. Quantum state tomography based on nonadiabatic holonomic single-qubit gates. Bare states $|1\rangle$, $|2\rangle$, and $|4\rangle$ form a Λ configuration where $|1\rangle$, $|2\rangle$ and $|1\rangle$, $|4\rangle$ are coupled by the π- and σ^{-}-transition microwaves, respectively.

4. Quantum state tomography and measurement errors

In this section we will introduce how to obtain the tomography of the pseudospin spanned by $|2\rangle$ and $|4\rangle$. By utilizing the complete control of the system through microwaves, we will utilize the nonadiabatic holonomic single-qubit gates to achieve quantum state tomography. We consider a three-level system composed of $\{|2\rangle, |1\rangle, |4\rangle\}$ as illustrated in Fig. 6. The interaction Hamiltonian in the rotating frame will take the form [11].

$$H_{nd} = \Omega_{21}(t)e^{i\varphi_2}|2\rangle\langle 1| + \Omega_{41}(t)e^{i\varphi_4}|4\rangle\langle 1| + \text{H.c.} \quad \text{(A3)}$$

By parametrizing $\Omega_{21} = \Omega_{nd}\sin\theta_{nd}$ and $\Omega_{41} = \Omega_{nd}\sin\theta_{nd}$ with $\varphi_{nd} = \varphi_2 - \varphi_4 + \pi$ and $\Omega_{nd} = \sqrt{\Omega_{21}(t)^2 + \Omega_{41}(t)^2}$, the dynamics can be considered as the resonant coupling between the states $|b\rangle = \sin(\theta_{nd}/2)e^{-i\varphi}|2\rangle - \cos(\theta_{nd}/2)|4\rangle$ and $|1\rangle$, while the dark eigenstate $|d\rangle = \cos(\theta_{nd}/2)|2\rangle + \sin(\theta_{nd}/2)e^{i\varphi}|4\rangle$ is decoupled. Hence, when the condition for cyclic evolution is satisfied (i.e., $\int_0^{\tau}\Omega_{nd}dt = \pi$, where τ is the evolution period), a specific single-qubit gate can be obtained for the basis states $|2\rangle$ and $|4\rangle$, as shown by

$$U_{\text{tomo}} = \begin{pmatrix} \cos\theta_{nd} & \sin\theta_{nd}e^{-i\varphi} \\ \sin\theta_{nd}e^{i\varphi} & -\cos\theta_{nd} \end{pmatrix}. \quad \text{(A4)}$$

By choosing specific parameters in Eq. (A4), i.e., $\theta_{nd} = \pi/2$ and $\varphi_{nd} = 0$, the σ_y operation can be realized, while

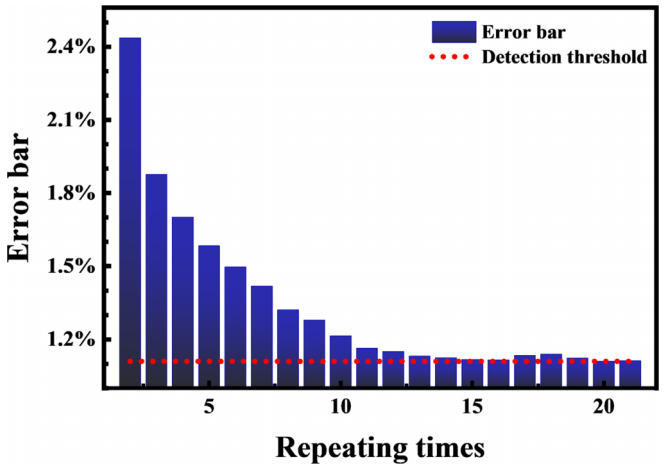

FIG. 7. Error bars on the experimental data decrease as the number of measurements increases. As the number of measurements approaches a certain threshold, the error bars converge towards a value of 0.011. This value can be used as a criterion for determining the minimum detectable signal.

$\theta_{nd} = \pi/2$ and $\varphi_{nd} = \pi/2$ correspond to the σ_x operation. In our experiment, we need to measure three components of the Bloch vector, namely, $\langle\sigma_{x,y,z}\rangle$. The expectation value of $\langle\sigma_z\rangle$ can be determined by measuring the atomic population difference between states $|2\rangle$ and $|4\rangle$. In order to measure the expectation value of Bloch vectors $\langle\sigma_x\rangle$ and $\langle\sigma_y\rangle$, a $\pi/2$ microwave pulse is applied with a phase of either 0 or $\pi/2$. This pulse is used to rotate the Bloch vector accordingly before the population difference measurement is taken. We now discuss measurement errors. As depicted in Fig. 7, the error bars for population P_4 decrease as the number of measurements increase. Eventually, the error bars converge to a value of 0.011, which can be considered as the threshold for detecting the smallest possible signal.

[1] D. W. Zhang, Y. Q. Zhu, Y. X. Zhao, H. Yan, and S. L. Zhu, Topological quantum matter with cold atoms, Adv. Phys. **67**, 253 (2018).

[2] M. Z. Hasan and C. L. Kane, *Colloquium*: Topological insulators, Rev. Mod. Phys. **82**, 3045 (2010).

[3] X. L. Qi and S. C. Zhang, Topological insulators and superconductors, Rev. Mod. Phys. **83**, 1057 (2011).

[4] M. V. Berry, Quantal phase factors accompanying adiabatic changes, Proc. R. Soc. London A **392**, 45 (1984).

[5] R. Jackiw and C. Rebbi, Vacuum Periodicity in a Yang-Mills Quantum Theory, Phys. Rev. Lett. **37**, 172 (1976).

[6] R. Jackiw, Introduction to the Yang-Mills quantum theory, Rev. Mod. Phys. **52**, 661 (1980).

[7] T. T. Wu and C. N. Yang, Concept of nonintegrable phase factors and global formulation of gauge fields, Phys. Rev. D **12**, 3845 (1975).

[8] J.-Z. Li, C.-J. Zou, Y.-X. Du, Q.-X. Lv, W. Huang, Z.-T. Liang, D.-W. Zhang, H. Yan, S. Zhang, and S.-L. Zhu, Synthetic Topological Vacua of Yang-Mills Fields in Bose-Einstein Condensates, Phys. Rev. Lett. **129**, 220402 (2022).

[9] F. Wilczek and A. Zee, Appearance of Gauge Structure in Simple Dynamical Systems, Phys. Rev. Lett. **52**, 2111 (1984).

[10] L. M. Duan, J. I. Cirac, and P. Zoller, Geometric manipulation of trapped ions for quantum computation, Science **292**, 1695 (2001).

[11] E. Sjöqvist, D. M. Tong, L. M. Andersson, B. Hessmo, M. Johansson, and K. Singh, Non-adiabatic holonomic quantum computation, New J. Phys. **14**, 103035 (2012).

[12] A. A. Abdumalikov, Jr. J. M. Fink, K. Juliusson, M. Pechal, S. Berger, A. Wallraff, and S. Filipp, Experimental realization of non-Abelian non-adiabatic geometric gates, Nature (London) **496**, 482 (2013).

[13] C. Zu, W.-B. Wang, L. He, W.-G. Zhang, C.-Y. Dai, F. Wang, and L.-M. Duan, Experimental realization of universal geometric quantum gates with solid-state spins, Nature (London) **514**, 72 (2014).

[14] K. Toyoda, K. Uchida, A. Noguchi, S. Haze, and S. Urabe, Realization of holonomic single-qubit operations, Phys. Rev. A **87**, 052307 (2013).

[15] F. Leroux, K. Pandey, R. Rehbi, F. Chevy, C. Miniatura, B. Grémaud, and D. Wilkowski, Non-Abelian adiabatic geometric transformations in a cold strontium gas, Nat. Commun. **9**, 3580 (2018).

[16] M. Boguslawski, M. Barrios, L. Xin, and M. S. Chapman, Exploring Non-Abelian Geometric Phases in Spin-1 Ultracold Atoms, Phys. Rev. Lett. **123**, 173202 (2019).

[17] V. Gritsev and A. Polkovnikov, Dynamical quantum Hall effect in the parameter space, Proc. Natl. Acad. Sci. USA **109**, 6457 (2012).

[18] M. D. Schroer, M. H. Kolodrubetz, W. F. Kindel, M. Sandberg, J. Gao, M. R. Vissers, D. P. Pappas, A. Polkovnikov, and K. W. Lehnert, Measuring a Topological Transition in an Artificial Spin-1/2 System, Phys. Rev. Lett. **113**, 050402 (2014).

[19] P. Roushan, C. Neill, Y. Chen, M. Kolodrubetz, C. Quintana, N. Leung, M. Fang, R. Barends, B. Campbell, Z. Chen *et al.*, Observation of topological transitions in interacting quantum circuits, Nature (London) **515**, 241 (2014).

[20] X. Tan, D.-W. Zhang, W. Zheng, X. Yang, S. Song, Z. Han, Y. Dong, Z. Wang, D. Lan, H. Yan, S.-L. Zhu, and Y. Yu, Experimental Observation of Tensor Monopoles with a Superconducting Qudit, Phys. Rev. Lett. **126**, 017702 (2021).

[21] X. Tan, D.-W. Zhang, W. Zheng, X. Yang, S. Song, Z. Han, Y. Dong, Z. Wang, D. Lan, H. Yan, S.-L. Zhu, and Y. Yu, Experimental Measurement of the Quantum Metric Tensor and Related Topological Phase Transition with a Superconducting Qubit, Phys. Rev. Lett. **122**, 210401 (2019).

[22] A. Gianfrate, O. Bleu, L. Dominici, V. Ardizzone, M. De Giorgi, D. Ballarini, G. Lerario, K. W. West, L. N. Pfeiffer, D. D. Solnyshkov, D. Sanvitto, and G. Malpuech, Measurement of the quantum geometric tensor and of the anomalous Hall drift, Nature (London) **578**, 381 (2020).

[23] M. Yu, P. Yang, M. Gong, Q. Cao, Q. Lu, H. Liu, S. Zhang, M. B. Plenio, F. Jelezko, T. Ozawa, N. Goldman, and J. Cai, Experimental measurement of the quantum geometric tensor using coupled qubits in diamond, Natl. Sci. Rev. **7**, 254 (2020).

[24] X. Tan, Topological Maxwell Metal Bands in a Superconducting Qutrit, Phys. Rev. Lett. **120**, 130503 (2018).

[25] S.-L. Zhu, Geometric phases and quantum phase transitions, Int. J. Mod. Phys. B **22**, 561 (2008).

[26] M. Kolodrubetz, Measuring the Second Chern Number from Nonadiabatic Effects, Phys. Rev. Lett. **117**, 015301 (2016).

[27] S. Sugawa, F. Salces-Carcoba, A. R. Perry, Y. Yue, and I. B. Spielman, Second Chern number of a quantum-simulated non-Abelian Yang monopole, Science **360**, 1429 (2018).

[28] X. D. Zhang, Z. D. Wang, L. B. Hu, Z. M. Zhang, and S. L. Zhu, Detecting unambiguously non-Abelian geometric phases with trapped ions, New J. Phys. **10**, 043031 (2008).

[29] R. Tycko, Adiabatic Rotational Splittings and Berry's Phase in Nuclear Quadrupole Resonance, Phys. Rev. Lett. **58**, 2281 (1987).

[30] P. J. Leek, J. M. Fink, A. Blais, R. Bianchetti, M. Göppl, J. M. Gambetta, D. I. Schuster, L. Frunzio, R. J. Schoelkopf, and A. Wallraff, Observation of Berry's phase in a solid-state qubit, Science **318**, 1889 (2007).

[31] Y. Yang, C. Peng, D. Zhu, H. Buljan, J. D. Joannopoulos, B. Zhen, and M. Soljačić, Synthesis and observation of non-Abelian gauge fields in real space, Science **365**, 1021 (2019).

[32] S. Sugawa, F. Salces-Carcoba, Y. Yue, A. Putra, and I. B. Spielman, Wilson loop and Wilczek-Zee phase from a non-Abelian gauge field, npj Quantum Inf. **7**, 144 (2021).

[33] J. Ruseckas, G. Juzeliūnas, P. Öhberg, and M. Fleischhauer, Non-Abelian Gauge Potentials for Ultracold Atoms with Degenerate Dark States, Phys. Rev. Lett. **95**, 010404 (2005).

[34] G. Juzeliūnas, J. Ruseckas, M. Lindberg, L. Santos, and P. Öhberg, Quasirelativistic behavior of cold atoms in light fields, Phys. Rev. A **77**, 011802(R) (2008).

[35] S.-L. Zhu, D.-W. Zhang, and Z. D. Wang, Delocalization of Relativistic Dirac Particles in Disordered One-Dimensional Systems and Its Implementation with Cold Atoms, Phys. Rev. Lett. **102**, 210403 (2009).

[36] D. W. Zhang, Z. D. Wang, and S. L Zhu, Relativistic quantum effects of Dirac particles simulated by ultracold atoms, Front. Phys. **7**, 31 (2012).

[37] A. M. Polyakov, *Gauge Fields and Strings* (Harwood, New York, 1987).

[38] Q.-X. Lv, Y.-X. Du, Z.-T. Liang, H.-Z. Liu, J.-H. Liang, L.-Q. Chen, L.-M. Zhou, S.-C. Zhang, D.-W. Zhang, B.-Q. Ai, H. Yan, and S.-L. Zhu, Measurement of Spin Chern Numbers in Quantum Simulated Topological Insulators, Phys. Rev. Lett. **127**, 136802 (2021).

[39] R. G. Unanyan, B. W. Shore, and K. Bergmann, Laser-driven population transfer in four-level atoms: Consequences of non-Abelian geometrical adiabatic phase factors, Phys. Rev. A **59**, 2910 (1999).

[40] S. L. Zhu and Z. D. Wang, Implementation of Universal Quantum Gates Based on Nonadiabatic Geometric Phases, Phys. Rev. Lett. **89**, 097902 (2002).

[41] Y. X. Du, B. J. Liu, Q. X. Lv, X. D. Zhang, H. Yan, and S. L. Zhu, Degenerate eigensubspace in a triangle-level system and its geometric quantum control, Phys. Rev. A **96**, 012333 (2017).

[42] Y. Xu, W. Cai, Y. Ma, X. Mu, L. Hu, T. Chen, H. Wang, Y. P. Song, Z.-Y. Xue, Z.-q. Yin, and L. Sun, Single-Loop Realization of Arbitrary Nonadiabatic Holonomic Single-Qubit Quantum Gates in a Superconducting Circuit, Phys. Rev. Lett. **121**, 110501 (2018).

[43] T. Chen and Z. Y. Xue, Nonadiabatic Geometric Quantum Computation with Parametrically Tunable Coupling, Phys. Rev. Appl. **10**, 054051 (2018).

[44] S. Li and Z. Y. Xue, Dynamically Corrected Nonadiabatic Holonomic Quantum Gates, Phys. Rev. Appl. **16**, 044005 (2021).

[45] Y. Liang, P. Shen, T. Chen, and Z.-Y. Xue, Nonadiabatic holonomic quantum computation and its optimal control, Sci. China Inf. Sci. **66**, 180502 (2023).

[46] N. V. Vitanov and B. M. Garraway, Landau-Zener model: Effects of finite coupling duration, Phys. Rev. A **53**, 4288 (1996).

[47] The final population in states $|1\rangle$ and $|3\rangle$ vanishes according to the manipulation.

[48] The $\langle\sigma_z\rangle$ component of **F** is obtained by normalized detection of the population in $|2\rangle$ and $|4\rangle$. The $\langle\sigma_{x\,(y)}\rangle$ component of **F** is obtained by measuring $\langle\sigma_z\rangle$ after a $(\pi/2)_{x\,(y)}$ pulse along the x (y) axis. The measurement is based on the nonadiabatic holonomic quantum computation [11].

[49] M. Demirplak and S. A. Rice, Adiabatic population transfer with control fields, J. Phys. Chem. A **107**, 9937 (2003).

[50] M. Demirplak and S. A. Rice, Assisted adiabatic passage revisited, J. Phys. Chem. B **109**, 6838 (2005).

[51] M. V. Berry, Transitionless quantum driving, J. Phys. A: Math. Theor. **42**, 365303 (2009).

[52] X. Chen, I. Lizuain, A. Ruschhaupt, D. Guery-Odelin, and J. G. Muga, Shortcut to Adiabatic Passage in Two- and Three-Level Atoms, Phys. Rev. Lett. **105**, 123003 (2010).

[53] M. G. Bason, M. Viteau, N. Malossi, P. Huillery, E. Arimondo, D. Ciampini, R. Fazio, V. Giovannetti, R. Mannella, and O. Morsch, High-fidelity quantum driving, Nat. Phys. **8**, 147 (2012).

[54] Y. X. Du, Z.-T. Liang, Y.-C. Li, X.-X. Yue, Q.-X. Lv, W. Huang, X. Chen, H. Yan, and S.-L. Zhu, Experimental realization of stimulated Raman shortcut-to-adiabatic passage with cold atoms, Nat. Commun. **7**, 12479 (2016).